



## **Laser-based Powder Bed Fusion of dispersion strengthened CoCrNi by ex-situ addition of TiN**

Downloaded from: <https://research.chalmers.se>, 2024-04-19 13:30 UTC

Citation for the original published paper (version of record):

Malladi, S., Cordova Gonzalez, L., Guo, S. et al (2022). Laser-based Powder Bed Fusion of dispersion strengthened CoCrNi by ex-situ addition of TiN. *Procedia CIRP*, 111: 368-372.  
<http://dx.doi.org/10.1016/j.procir.2022.08.168>

N.B. When citing this work, cite the original published paper.

12th CIRP Conference on Photonic Technologies [LANE 2022], 4-8 September 2022, Fürth, Germany

## Laser-based Powder Bed Fusion of dispersion strengthened CoCrNi by ex-situ addition of TiN

Sri Bala Aditya Malladi<sup>a,\*</sup>, Laura Cordova<sup>a</sup>, Sheng Guo<sup>a</sup>, Lars Nyborg<sup>a</sup>

<sup>a</sup>*Department of Industrial and Materials Science, Chalmers University of Technology, Göteborg, Sweden*

\* Corresponding author. Tel.: +46-734783233; E-mail address: [malladi@chalmers.se](mailto:malladi@chalmers.se)

### Abstract

In this study, metal matrix composites (MMC) of a CoCrNi medium entropy alloy (MEA) reinforced with titanium nitride (TiN) nano-sized particles were designed for production by laser-based powder bed fusion (LB-PBF). Two different additions, 0.5 wt% and 5 wt% of TiN nano-sized particles, were mixed with CoCrNi using tumbling and ball milling, respectively. The results suggest that although the powder morphology is not significantly affected by the TiN addition, the processability of CoCrNi-5 wt% TiN is worse than that of CoCrNi and CoCrNi-0.5 wt% TiN. The hardness of CoCrNi, originally 278 HV, is enhanced by addition of 0.5% and 5% TiN to 309 HV and 357 HV respectively. This hardening is mainly due to the presence of reinforcement particles in the matrix. The work presented here shows promising processability of MMC based on MEAs by LB-PBF, as well as the beneficial effect of the reinforcement phase on the mechanical properties of MEAs.

© 2022 The Authors. Published by Elsevier B.V.

This is an open access article under the CC BY-NC-ND license (<https://creativecommons.org/licenses/by-nc-nd/4.0>)

Peer-review under responsibility of the international review committee of the 12th CIRP Conference on Photonic Technologies [LANE 2022]

**Keywords:** Additive Manufacturing; Laser-based powder bed fusion; CoCrNi; Medium entropy alloys; Titanium nitride; Metal matrix composites

### 1. Introduction

Additive manufacturing (AM) processes have rapidly revolutionized the manufacturing landscape over the past few decades. Among the AM processes, laser-based powder bed fusion (LB-PBF) has grown from rapid prototyping to manufacturing for applications in high performance aerospace and automobile components [1,2]. This development in the technology also resulted in an improvement in the material portfolio either by adapting the existing conventional materials or by developing new materials that cater to LB-PBF processing conditions.

Metal matrix composites (MMC) are one class of materials which consist of a continuous metallic phase as the matrix and a reinforcement phase. One important characteristic of the MMC is that, unlike conventional alloys, the combination of the matrix and the reinforcement phase remain distinct throughout the processing. This unique combination of soft metallic phase

with a hard reinforcement phase improves the mechanical properties in a manner different to any other class of materials [3]. Reinforcing the metallic phase with a discontinuous reinforcement phase also helps in achieving isotropic properties due to the ability from the reinforcement phase to inhibit the dislocation motion, finding wide applications of MMC in the aerospace and automobile industries [4–6].

Manufacturing of MMC is traditionally done by i) liquid-state processes (for example, casting), ii) solid-state processing (for example, powder metallurgy) or deposition processing (for example, vapor deposition) [3,7]. However, traditional routes for manufacturing of MMC are typically expensive and could result in issues such as segregation and low densification [8–10]. With the recent advances in the field of AM and especially in LB-PBF, there is a growing interest in the AM of MMC owing to its unique advantage of near-net shape manufacturing of complex geometries, thereby reducing the costs for post processing such as machining.

High entropy alloys (HEAs) and medium entropy alloys (MEAs) are novel classes of alloys, in which the formation of simple solid solution phases can be stabilized by the configurational entropy. Accompanying with the increasing interest in HEAs, there is also a growing interest in reinforced composites based on HEAs, to further enhance the mechanical properties of HEAs using the traditional manufacturing routes [11,12]. However, not much work has been reported on the LB-PBF fabrication of MMC with an MEA as the matrix. Equiatomic CoCrNi belongs to MEAs and has recently attracted increasing attention due to its excellent phase stability and mechanical properties [13–15].

The present work demonstrates the processability, densification, microstructure, distribution of the reinforcement phase in the CoCrNi MEA, as the metallic phase and the resulting influence of the ex-situ addition of 0.5 wt% and 5 wt% of titanium nitride (TiN) nano-sized particles TiN particles, as the reinforcement phase, on the mechanical properties of the CoCrNi-TiN MMC.

## 2. Materials and Methods

Pre-alloyed gas atomized equiatomic CoCrNi MEA powder, with the particle size distribution (PSD) between 15  $\mu\text{m}$  and 45  $\mu\text{m}$  supplied by Höganäs AB, were utilized in this work. 0.5 wt% and 5 wt% of TiN nano-sized particles with an average size of 80 nm (US Research Nanomaterials, Inc) were added to the MEA powders. Mixing of the alloy powders with 0.5 wt% TiN particles was conducted in a tumbler placed inside a glove box, while mixing of the alloy powders with 5 wt% TiN particles was carried out using ball milling with a powder to ball ratio of 1:5 for 15 minutes. The PSD was measured by laser diffraction using a Mastersizer 3000 equipment. The measurement was repeated 5 times for each powder batch in order to get an accurate estimate of nanosized and micron sized particle size distributions. The Brunauer-Emmett-Teller (BET) specific surface area ( $S_A$ ) was measured by a Micromeritics Gemini VII surface area analyzer. The powder was dried in nitrogen at 200 °C for 2 hours, before the flowability behavior was studied using a revolution powder analyzer (RPA) from Mercury Scientific. An equal sample size of 110 grams of each powder composition was taken. The avalanche angle was measured using the multi-flow method varying the speed from 1 to 50 revolutions per minute (RPM) in which 75 avalanches per speed were analyzed. The tap density values were obtained by averaging ten cycles of tapping and vibration.

All the three materials (without and with 0.5 wt% and 5 wt% of TiN) were printed by means of LB-PBF using an EOS-M100 machine equipped with a 200 W Yb-fiber laser with a spot size of 40  $\mu\text{m}$ . All the materials were printed with a 20  $\mu\text{m}$  layer thickness in Argon atmosphere with scan rotation of 67° was used between the subsequent layers. For the purpose of design of experiments (DoE), cubes of 10 mm x 10 mm x 10 mm were produced with varying printing parameters.

The as-printed samples were then removed from the build plate and sectioned parallel to the building direction, hot-mounted in a conductive resin. The mounted samples were then polished to mirror finish for microstructural analysis. The densification of the printed samples was measured by image

analysis of the stitched optical microscopy images using the Zeiss Axiovision 7 software, in which the entire cross sections of the printed samples were covered. The microstructural characterization and compositional analysis were performed using the Leo Gemini 450 scanning electron microscope (SEM) equipped with an X-Max energy dispersive spectroscopy (EDS) detector. All the three materials were evaluated for hardness using a Struers Durascan 70 G5 tester at 1 kgf load for a dwell time of 15 seconds.

## 3. Results and Discussion

### 3.1. Powder properties

Surface characteristics of the virgin and mixed powder of all the three variants are shown in Fig. 1. The virgin CoCrNi powder particles show a spherical morphology with visible grain boundaries on the surface, and some very fine satellites are attached to the particles as shown in Fig. 1a. Powder particles from CoCrNi - 0.5 wt% TiN also show a spherical morphology, with TiN particles homogeneously coated on the surface of the CoCrNi powder as shown in Fig. 1b. CoCrNi - 5 wt% TiN particles, however, show agglomerates of the TiN particles both on the surface of the CoCrNi particles and near them as seen from Fig. 1c. The PSD of powders for all the three powder variants looks rather similar, with D50 circa 32  $\mu\text{m}$  as seen in Fig. 1d. The PSD of CoCrNi - 5 wt% TiN shows a small peak for particle sizes between 2 and 8  $\mu\text{m}$  (inset), most probably due to agglomerates of the TiN particles, as also observed in the SEM images (Fig. 1c).

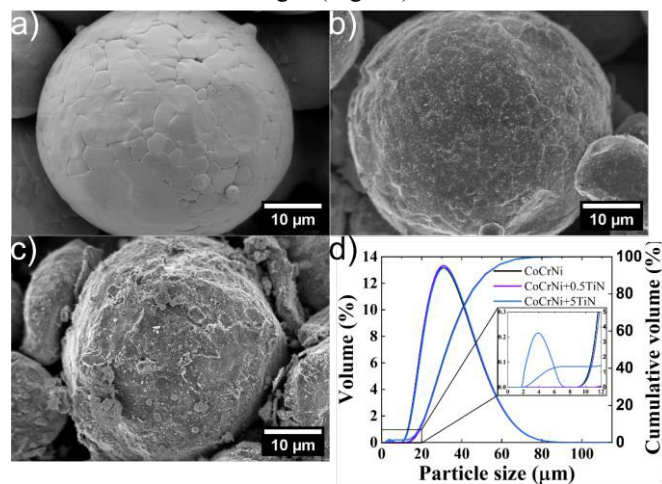


Fig. 1 Scanning electron micrographs of a) Virgin CoCrNi b) CoCrNi mixed with 0.5 wt% TiN c) CoCrNi mixed with 5 wt% TiN and d) particle size distribution (PSD) of all three variants.

The flow behavior determines the quality of the powder layer deposited onto the build plate, and the tap density shows how the powder is closely packed for full melting by the laser beam. Fig. 2 shows the avalanche angle values obtained with the RPA, specific surface area ( $S_A$ ) and tap density for each powder composition. The best flowing powder is the virgin CoCrNi powder, followed by the CoCrNi - 0.5 wt% TiN while the variant having 5 wt% added TiN shows the worst behaviour. The flow behavior worsens with the increasing content of TiN nano-sized particles due to an increase in  $S_A$ .

Similarly, the tap density decreases with the addition of TiN nano-sized particles and subsequent increase in  $S_A$  (Fig. 1b), with the decrease being marginal with 0.5 wt% TiN addition. It can be summarized that adding small amounts of TiN nano-sized particles, 0.5 wt% in this case, does not significantly affect the powder flowability and tap density.

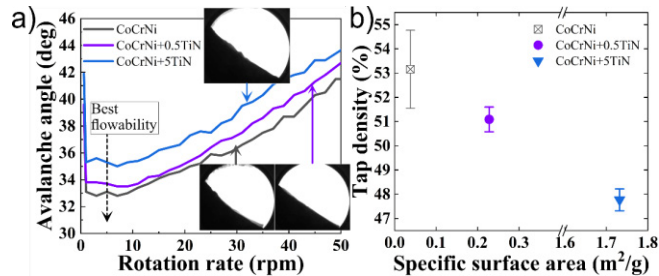


Fig. 2 (a) Flow behavior of the virgin and mixed powder tested with the RPA in the dynamic regime from 1-50 RPM. The powder avalanche morphology is represented by binary images. (b) Tap density versus specific surface area.

### 3.2. Processability and microstructural characterization

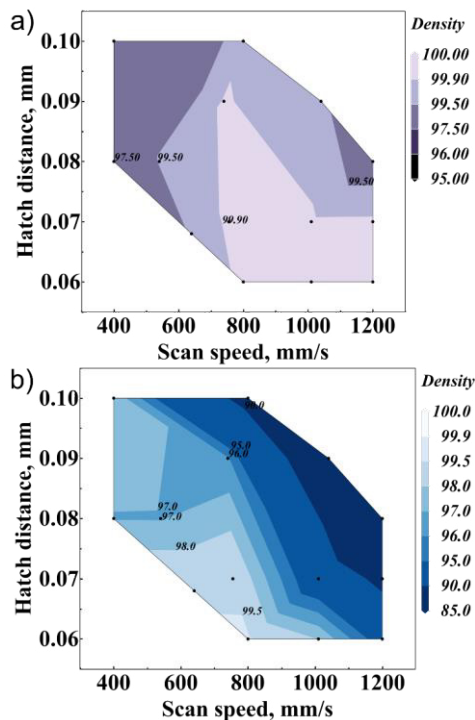


Fig. 3. Contour plots showing the influence of hatch distance and scan speed for parts printed at a constant power of 110W as a function of measured relative densities for a) CoCrNi + 0.5 wt% TiN and b) CoCrNi + 5 wt% TiN.

Fig. 3 shows the contour plots obtained from the DoE analysis of the relative densities of as-printed samples. The CoCrNi - 0.5 wt% TiN powder shows better processability with a larger process window (as shown in Fig. 3a), which is critical for high productivity in LB-PBF. From the process window of the CoCrNi - 5 wt% TiN powder (Fig. 3b), it can be concluded that a high density is achieved at low scanning speed and short hatch distances, indicating that a higher energy input is needed to achieve a high density, when the amount of reinforcement phase is increased. This could be due to the differences in the thermal properties between the TiN phase and the CoCrNi metallic phase and high melting point of TiN (2950 °C)

necessitating the high energy input to achieve full densification [16,17].

SEM backscattered images of the as-printed samples are shown in Fig. 4. The addition of TiN nano-sized particles did not have any noticeable influence on the microstructure. All three variants, with and without TiN addition, show a typical LB-PBF microstructure with a mixture of epitaxially grown long columnar grains together with some small equiaxed grains along the building direction. Small grains observed in the CoCrNi material could be due to the 67° scan rotation between the subsequent layers which disrupts the solidification conditions that facilitate the epitaxial growth of columnar grains [18]. The presence of dark particles in the CoCrNi - 0.5 wt% TiN and CoCrNi - 5 wt% TiN suggests that the added TiN particles are rather homogeneously distributed in the CoCrNi matrix, and the role of different TiN additions could be clearly reflected in the microstructure. Compared to the lower TiN content which results in finer dark particles, the higher TiN content leads to the agglomerates of originally 80 nm sized particles, possibly formed during the ball milling process. Still, in both cases there is evidence that the distribution of non-agglomerated TiN particles is much finer, with average distance between TiN particles in the matrix much smaller than that of the CoCrNi particle size as a result of redistribution occurring during the LB-PBF process.

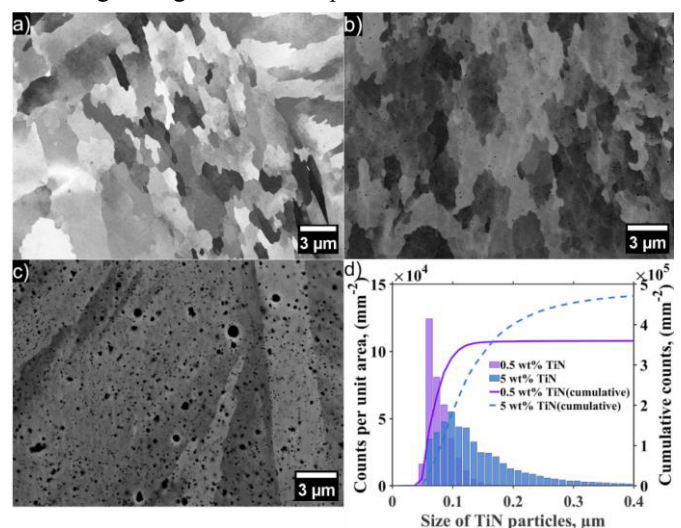


Fig. 4. SEM backscattered electron images of as-printed samples of a) CoCrNi, b) CoCrNi - 0.5 wt% TiN and c) CoCrNi - 5 wt% TiN samples and d) PSD of TiN particles in both TiN containing materials as measured from the feature analysis.

Fig. 5 shows an EDS line scan on one of the particles in the as-printed CoCrNi - 5 wt% TiN. The presence of a core-shell structure with an oxide core and a nitride shell was observed. Such core-shell structure was not observed in the CoCrNi - 0.5 wt % powder TiN. The reasoning behind could be that due to ball milling of the CoCrNi - 5 wt% TiN powder was performed at atmospheric conditions, and the temperature during the milling process could easily exceed 100 °C, this resulted in the surface oxidation of the TiN nano-sized particles. Though the added TiN particles are 99.7% pure, they readily oxidize resulting in the formation of a thin oxide film on the surface even at room temperature [19–21]. During the printing process, the high energy input used for achieving full densification



might have caused either partial or full melting of some of these particles as seen in Ref. [22,23]. During the solidification process, titanium oxides nucleate first, which act as nucleating sites for titanium nitrides, leading to the core-shell structure.

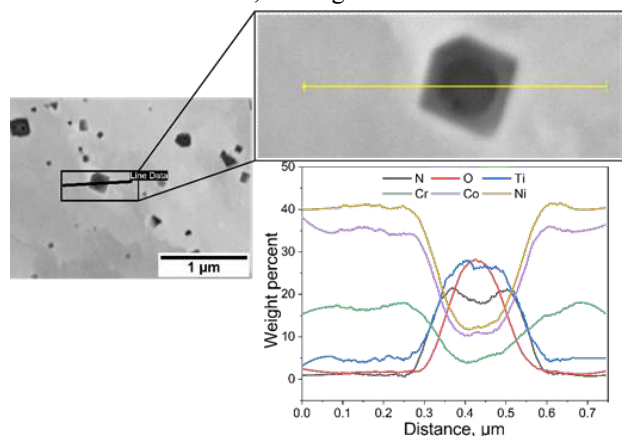


Fig. 5. EDS line scan analysis of TiN particle, showing the presence of oxygen rich core and nitrogen rich shell.

Additionally, the increase in TiN content from 0.5 wt% to 5 wt% has also influenced the number and size distribution of these reinforcement phases in the CoCrNi matrix. The classification of the particles was done based on the elemental data obtained from the EDS analysis. Particles containing only nitrogen or both nitrogen and oxygen were considered for the feature analysis. Based on this classification, the TiN PSD in the matrix of LB-PBF samples is shown in Fig. 4d.

The average size of the TiN particles as measured from the feature analysis for CoCrNi - 0.5 wt% TiN material is circa 80 nm, close to that of the starting TiN size, while the average size of particles for CoCrNi - 5 wt% is circa 140 nm. Even with the increased TiN particle size, the number density (per unit area) in CoCrNi - 5 wt% TiN material is circa 40 % greater than that in CoCrNi - 0.5 wt%.

### 3.3. Mechanical properties

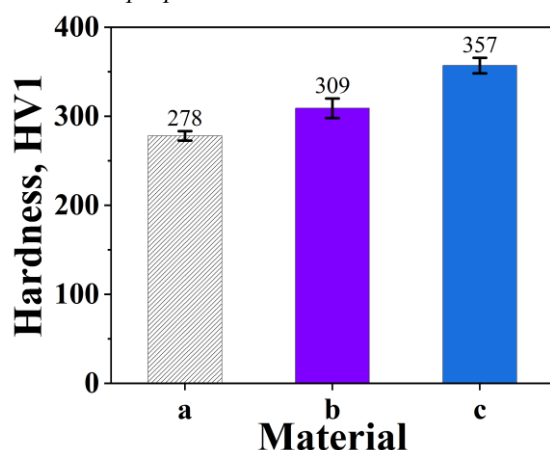


Fig. 6. Hardness plot of as-printed samples of a) CoCrNi, b) CoCrNi - 0.5 wt% TiN and c) CoCrNi - 5 wt% TiN, showing the influence from the TiN reinforcement.

Hardness tests were performed on the as-printed samples of all three variants of the alloy, in order to understand the

influence of the TiN reinforcement the results are shown in Fig. 6. CoCrNi in the as-printed state exhibited a hardness of 278 HV. Addition of TiN to the CoCrNi clearly increased the hardness, with CoCrNi - 0.5 wt% TiN and CoCrNi - 5 wt% TiN showing a hardness of 309 HV and 357 HV respectively. This shows a stronger influence from the number density, than that from the average TiN particle size.

## 4. Conclusions

The aim of this study was to develop new MMC based on a CoCrNi MEA reinforced with TiN nano-sized particles, and to demonstrate their processability by LB-PBF. Following conclusions can be drawn from this study:

- Addition of 0.5 wt% and 5 wt% of TiN did not significantly influence the morphology of the CoCrNi MEA powder, although the CoCrNi - 5wt% TiN powder showed the presence of agglomerates formed during ball milling.
- The addition of TiN resulted in a decrease in flowability and tap density of the powders, which was more significant for the CoCrNi - 5 wt% TiN powder.
- The processability by LB-PBF was tested by running a DoE, which showed a wider process window for CoCrNi - 0.5 wt% TiN compared to CoCrNi - 5 wt% TiN. Higher energy input is essentially needed to achieve full densification with the increasing content of the reinforcement phase.
- The reinforcement phase is uniformly distributed in both CoCrNi - 0.5 wt% TiN and CoCrNi - 5 wt% TiN. CoCrNi-5wt% TiN showed a 10 times higher particle density compared to that in CoCrNi-0.5 wt% TiN.
- The hardness of as-printed CoCrNi, originally 278 HV, was enhanced by addition of 0.5 wt% and 5 wt% TiN to 309 HV and 357 HV, respectively.

The results achieved in this work demonstrate that LB-PBF is a promising technique to prepare MMC based on MEAs, with improved mechanical properties.

## Acknowledgements

This study was performed with support from Metalliska Material, one of the strategic innovation programmes of Vinnova, through the project, 'Design of novel materials and processes for next generation additive manufacturing' (2018-00803), European Union's Horizon 2020 research and innovation program (820774) within project MANUELA-Additive Manufacturing using Metal Pilot Line and Competence Centre for Additive Manufacture-Metal (CAM<sup>2</sup>) (2016-05175) and the Production Area of Advance at Chalmers. Höganäs AB is greatly acknowledged for their valuable support. The authors thank Mikael Eriksson from RISE IVF, Sweden.

## References

- [1] W.E. Frazier, Metal additive manufacturing: A review, *Journal of Materials Engineering and Performance*. 23 (2014) 1917–1928. <https://doi.org/10.1007/s11665-014-0958-z>.

- [2] D. Herzog, V. Seyda, E. Wycisk, C. Emmelmann, Additive manufacturing of metals, *Acta Materialia*. 117 (2016) 371–392. <https://doi.org/10.1016/j.actamat.2016.07.019>.
- [3] A. Evans, C. San Marchi, A. Mortensen, Metal Matrix Composites, in: *Metal Matrix Composites in Industry: An Introduction and a Survey*, Springer US, Boston, MA, 2003: pp. 9–38. [https://doi.org/10.1007/978-1-4615-0405-4\\_2](https://doi.org/10.1007/978-1-4615-0405-4_2).
- [4] V. Srinivasan, S. Kunjiappan, P. Ponnusamy Palanisamy, A brief review of carbon nanotube reinforced metal matrix composites for aerospace and defense applications, *International Nano Letters* 2021 11:4. 11 (2021) 321–345. <https://doi.org/10.1007/S40089-021-00328-Y>.
- [5] B.N. Anthony Palazotto, R. Run, G. Watt, Introduction to Metal Matrix Composites in Aerospace Applications, *Journal of Aerospace Engineering*. 1 (1988) 3–17. [https://doi.org/10.1061/\(ASCE\)0893-1321\(1988\)1:1\(3\)](https://doi.org/10.1061/(ASCE)0893-1321(1988)1:1(3)).
- [6] T. Parsonage, Beryllium metal matrix composites for aerospace and commercial applications, 16 (2013) 732–738. <https://doi.org/10.1179/026708300101508522>.
- [7] K.K. Chawla, Metal Matrix Composites, in: *Composite Materials: Science and Engineering*, Springer New York, New York, NY, 2012: pp. 197–248. [https://doi.org/10.1007/978-0-387-74365-3\\_6](https://doi.org/10.1007/978-0-387-74365-3_6).
- [8] S. Chen, Y. Tong, P.K. Liaw, Additive manufacturing of high-entropy alloys: A review, *Entropy*. 20 (2018). <https://doi.org/10.3390/e20120937>.
- [9] A. Ostovari Moghaddam, N.A. Shaburova, M.N. Samodurova, A. Abdollahzadeh, E.A. Trofimov, Additive manufacturing of high entropy alloys: A practical review, *Journal of Materials Science & Technology*. 77 (2021) 131–162. <https://doi.org/10.1016/J.JMST.2020.11.029>.
- [10] Y. Brif, M. Thomas, I. Todd, The use of high-entropy alloys in additive manufacturing, *Scripta Materialia*. 99 (2015) 93–96. <https://doi.org/10.1016/j.scriptamat.2014.11.037>.
- [11] D. Yim, P. Sathiyamoorthi, S.J. Hong, H.S. Kim, Fabrication and mechanical properties of TiC reinforced CoCrFeMnNi high-entropy alloy composite by water atomization and spark plasma sintering, *Journal of Alloys and Compounds*. 781 (2019) 389–396. <https://doi.org/10.1016/J.JALLCOM.2018.12.119>.
- [12] Ł. Rogal, D. Kalita, A. Tarasek, P. Bobrowski, F. Czerwinski, Effect of SiC nano-particles on microstructure and mechanical properties of the CoCrFeMnNi high entropy alloy, *Journal of Alloys and Compounds*. 708 (2017) 344–352. <https://doi.org/10.1016/J.JALLCOM.2017.02.274>.
- [13] Z. Zhang, H. Sheng, Z. Wang, B. Gludovatz, Z. Zhang, E.P. George, Q. Yu, S.X. Mao, R.O. Ritchie, Dislocation mechanisms and 3D twin architectures generate exceptional strength-ductility-toughness combination in CrCoNi medium-entropy alloy, *Nature Communications* 2017 8:1. 8 (2017) 1–8. <https://doi.org/10.1038/ncomms14390>.
- [14] P. Niu, R. Li, K. Gan, T. Yuan, S. Xie, C. Chen, Microstructure, Properties, and Metallurgical Defects of an Equimolar CoCrNi Medium Entropy Alloy Additively Manufactured by Selective Laser Melting, *Metallurgical and Materials Transactions A* 2021 52:2. 52 (2021) 753–766. <https://doi.org/10.1007/S11661-020-06121-4>.
- [15] C.K. Soundararajan, H. Luo, D. Raabe, Z. Li, Hydrogen resistance of a 1 GPa strong equiatomic CoCrNi medium entropy alloy, *Corrosion Science*. 167 (2020) 108510. <https://doi.org/10.1016/J.CORSCI.2020.108510>.
- [16] E. Fereiduni, A. Ghasemi, M. Elbestawi, Selective laser melting of hybrid ex-situ/in-situ reinforced titanium matrix composites: Laser/powder interaction, reinforcement formation mechanism, and non-equilibrium microstructural evolutions, *Materials & Design*. 184 (2019) 108185. <https://doi.org/10.1016/J.MATDES.2019.108185>.
- [17] D.P.H. Hasselman, L.F. Johnson, Effective Thermal Conductivity of Composites with Interfacial Thermal Barrier Resistance, *Http://Dx.Doi.Org/10.1177/002199838702100602*. 21 (2016) 508–515. <https://doi.org/10.1177/002199838702100602>.
- [18] J.J. Marattukalam, D. Karlsson, V. Pacheco, P. Beran, U. Wiklund, U. Jansson, B. Hjörvarsson, M. Sahlberg, The effect of laser scanning strategies on texture, mechanical properties, and site-specific grain orientation in selective laser melted 316L SS, (2020). <https://doi.org/10.1016/j.matdes.2020.108852>.
- [19] H.-Y. Chen, F.-H. Lu, Oxidation behavior of titanium nitride films, *Journal of Vacuum Science & Technology A: Vacuum, Surfaces, and Films*. 23 (2005) 1006. <https://doi.org/10.1116/1.1914815>.
- [20] H.G. Tompkins, Oxidation of titanium nitride in room air and in dry O<sub>2</sub>, *Journal of Applied Physics*. 70 (1998) 3876. <https://doi.org/10.1063/1.349194>.
- [21] J. Sempere, R. Nomen, E. Serra, B. Sempere, D. Guglielmi, Thermal behavior of oxidation of TiN and TiC nanoparticles, *Journal of Thermal Analysis and Calorimetry*. 105 (2011) 719–726. <https://doi.org/10.1007/S10973-010-1214-X/FIGURES/18>.
- [22] M. Xia, A. Liu, Z. Hou, N. Li, Z. Chen, H. Ding, Microstructure growth behavior and its evolution mechanism during laser additive manufacture of in-situ reinforced (TiB+TiC)/Ti composite, *Journal of Alloys and Compounds*. 728 (2017) 436–444. <https://doi.org/10.1016/J.JALLCOM.2017.09.033>.
- [23] E. Fereiduni, A. Ghasemi, M. Elbestawi, Selective laser melting of hybrid ex-situ/in-situ reinforced titanium matrix composites: Laser/powder interaction, reinforcement formation mechanism, and non-equilibrium microstructural evolutions, *Materials & Design*. 184 (2019) 108185. <https://doi.org/10.1016/J.MATDES.2019.108185>.